Aerospace Science and Technology 168 (2026) 111087

Contents lists available at ScienceDirect

Aerospace Science and Technology

journal homepage: www.elsevier.com/locate/aescte

# Predicting the ascent of high-altitude tethered spherical balloons

Zhongwei Ni [a], Shiran Zhu [a], Shunan Dou [b], Jiawei Song [b], Ning An [a,c,*]

[a] Robotic Satellite Key Laboratory of Sichuan Province, Key Laboratory of Advanced Spatial Mechanism and Intelligent Spacecraft, Ministry of Education, School of Aeronautics and Astronautics, Sichuan University, Chengdu, 610065, People's Republic of China
[b] Jiangsu Ningshi Technology Co., Ltd, Wuxi, 214111, People's Republic of China
[c] Department of Civil, Environmental and Mechanical Engineering, University of Trento, Trento, 38122, Italy

ARTICLE INFO

Communicated by: Cheng Wang

*Keywords:*
Tethered balloon
Ascent behavior
Aerostat
Cable
Simulation

ABSTRACT

This paper presents a comprehensive analytical method for predicting the steady-state ascent path and tether profile of high-altitude tethered spherical balloons under varying wind conditions. The model incorporates altitude-dependent atmospheric properties and systematically accounts for all relevant external forces, including buoyancy, aerodynamic drag, weight, and payload. The tether is discretized into segments, and static equilibrium conditions are evaluated sequentially from the balloon attachment point down to the ground anchor, yielding the complete tether profile and internal tension distribution analytically. The method is validated against a finite element model based on continuous cable elements, demonstrating strong agreement and confirming its accuracy. The analytical model is implemented in MATLAB, and a computation code has been developed to automate the analysis process and support rapid design iteration. The method calculates the balloon's altitude and horizontal drift, as well as the tether's shape and tension distribution, based on specified system parameters and wind conditions. It also supports inverse design, enabling users to determine the required balloon size and tether length needed to achieve specified altitude and drift targets. The proposed framework is flexible and has the potential to be extended to other tethered aerostat configurations, such as helikites and streamlined airships, provided their aerodynamic characteristics are properly characterized.

## 1. Introduction

High-altitude tethered balloons are a typical class of lighter-than-air aircraft constrained by long tethers and have been widely adopted in various applications, including persistent surveillance, public safety, emergency communications, atmospheric research, and rapid disaster response [1–5]. These systems offer several advantages over satellite-based platforms, such as rapid deployment, lower cost, reduced latency, and localized coverage. Compared to ground-based communication systems such as communication towers, they also provide broader coverage, enhanced flexibility for repositioning, and improved signal propagation [6,7]. Particularly in recent years, tethered balloons have become an increasingly critical technology for emergency response, playing a vital role in addressing both natural and human-induced disasters. They enable the rapid deployment of broadband wireless communication networks and can deliver essential public safety services in the aftermath of catastrophic events. As such, tethered balloon systems are considered a key component of reliable public safety networks and can contribute significantly to saving lives [8–10].

Compared with streamlined aerostats, spherical balloons generate greater drag force, resulting in increased lateral drift and reduced operational altitude under crosswinds–both undesirable effects. However, due to their inherent simplicity, spherical aerostats remain a suitable choice for various applications [11]. Fig. 1 illustrates the tethered balloon system considered in this study. It consists of a vehicle-mounted mooring platform, a long tether, and a helium balloon. The balloon serves as a platform for carrying payloads such as communication systems, which provide connectivity to users in the surrounding area. The tether fulfills two functions: it acts as a structural link between the balloon and the winch system on the mooring platform, and it serves as an optical communication link between the balloon and the ground station. The winch system controls the tether by paying it out or retrieving it, enabling deployment and regulating the outhaul and inhaul of the tether during the balloon's ascent and descent. Key operational parameters of the system include the balloon's altitude and horizontal drift, which together determine the size and location of the effective coverage area. This area can be represented as a circular region on the horizontal plane, centered at the balloon's projected ground position. Its size depends primarily on the balloon's altitude and the communication range of the onboard system. Therefore, the balloon's altitude and drift are critical to system performance and constitute the primary focus of this study. In addition, the tether assumes a catenary-like shape due to the combined effects

* Corresponding author.
*E-mail address:* anning@scu.edu.cn (N. An).

https://doi.org/10.1016/j.ast.2025.111087
Received 15 August 2025; Received in revised form 29 September 2025; Accepted 12 October 2025
Available online 17 October 2025

**Nomenclature**

| | |
|---|---|
| $A_{\text{bal}}$ | Cross-sectional area of the balloon, $m^2$ |
| $A_{\text{tet}}$ | Cross-sectional area of the tether, $m^2$ |
| $A_i$ | Cross-sectional area of the $i$-th tether segment after deformation, $m^2$ |
| $C_D$ | Drag coefficient of the balloon |
| $C_{dni}$ | Normal drag coefficient of the $i$-th tether segment |
| $C_{d\tau i}$ | Tangential drag coefficient of the $i$-th tether segment |
| $d$ | Diameter of the tether, m |
| $D$ | Diameter of the balloon, m |
| $D_{ni}$ | Normal drag force on the $i$-th tether segment, N |
| $D_{\tau i}$ | Tangential drag force on the $i$-th tether segment, N |
| $E$ | Young's modulus of the tether material, Pa |
| $F_1$ | Horizontal force component at node I, N |
| $F_2$ | Vertical force component at node I, N |
| $F_3$ | Horizontal force component at node J, N |
| $F_4$ | Vertical force component at node J, N |
| $F_B$ | Buoyancy force acting on the balloon, N |
| $F_D$ | Aerodynamic drag force acting on the balloon, N |
| $g$ | Gravitational acceleration, $m/s^2$ |
| $H$ | Given altitude, m |
| $h$ | Altitude, m |
| $h_{\text{ref}}$ | Reference altitude for wind profile, m |
| $h_i$ | Midpoint height of the $i$-th tether segment, m |
| $K$ | Characteristic length parameter for tether discretization, m |
| $L$ | Initial, unstressed length of the tether, m |
| $L_e$ | Unstressed cable length, m |
| $L_e^{\text{def}}$ | Deformed cable length relative to the initial unstressed length, m |
| $L_e^x$ | Horizontal projection of the cable element, m |
| $L_e^y$ | Vertical projection of the cable element, m |
| $L_{\text{def}}$ | Deformed length of the tether, m |
| $m_{\text{env}}$ | Mass of the balloon envelope, kg |
| $m_{\text{load}}$ | Mass of the payload, kg |
| $m_i$ | Mass of the $i$-th tether segment, kg |
| $n$ | Total number of tether segments |
| $P$ | Air pressure, Pa |
| $P_0$ | Air pressure at sea level, Pa |
| $R$ | Universal gas constant for air, J/(mol·K) |
| $R_{\text{He}}$ | Gas constant for helium, J/(kg·K) |
| $Re_D$ | Reynolds number of the balloon |
| $Re_{di}$ | Reynolds number of the $i$-th tether segment |
| $S$ | Sutherland's constant, K |
| $T$ | Tension force at balloon-tether interface, N |
| $T_I$ | Cable tension magnitude at node I, N |
| $T_J$ | Cable tension magnitude at node J, N |
| $T_i$ | Tension at upper endpoint of $i$-th tether segment, N |
| $T_0$ | Temperature at sea level, K |
| $V$ | Volume of the spherical balloon, $m^3$ |
| $v$ | Wind speed, m/s |
| $v_{\text{ref}}$ | Reference wind speed, m/s |
| $w$ | Weight per unit length of cable, N/m |
| $W_{\text{bal}}$ | Total weight of the balloon and payload, N |
| $W_{\text{tet}}$ | Weight of the deployed tether, N |
| $X$ | Horizontal drift distance of the balloon, m |
| $\alpha$ | Wind profile exponent |
| $\theta$ | Angle between tether and vertical direction at balloon, rad |
| $\theta_i$ | Angle of $i$-th tether segment relative to vertical, rad |
| $\mu$ | Dynamic viscosity of air, Pa·s |
| $\mu_0$ | Dynamic viscosity of air at sea level, Pa·s |
| $\rho$ | Air density, $kg/m^3$ |
| $\rho_0$ | Air density at sea level, $kg/m^3$ |
| $\rho_{\text{He}}$ | Helium density, $kg/m^3$ |
| $\rho_{\text{tet}}$ | Density of tether material, $kg/m^3$ |
| $\Delta L_i$ | Elongation of $i$-th tether segment, m |
| FE | Finite element |
| UHMWPE | Ultra-high molecular weight polyethylene |
| HATASIM | High-Altitude Tethered Aerostat Simulation |
| ISA | International Standard Atmosphere |

of the balloon's pull, lateral wind forces, and its own weight. Both its shape and tension are crucial: the shape affects operational safety and effectiveness, particularly in environments with surrounding obstacles such as mountains, trees, or tall buildings, while the tension directly influences the structural integrity and safety of the system.

The main challenges in modeling a tethered balloon system stem from the complex interactions among the balloon, the tether, and atmospheric winds [12–14]. The balloon is typically represented as a body in equilibrium under the combined action of buoyancy, weight, aerodynamic drag, and tether tension. These forces are strongly dependent on altitude, since air density, pressure, and wind characteristics vary significantly with height. The tether is typically considered as a flexible cable with negligible bending stiffness, carrying only axial tension. Its shape is governed by the distribution of tension along its length, resulting in what is commonly referred to as a shape-finding problem in the analysis of tensile structures [15,16]. However, accurately modeling the long tether remains challenging and has been the focus of extensive research. Common approaches include discretizing the tether into lots of segments, employing lumped-mass models connected by springs and dampers, or using continuous finite element formulations. The Johns Hopkins University Applied Physics Laboratory [17] developed an analytical simulation of the two-dimensional dynamics of a tethered balloon subjected to a wide range of environmental conditions. The continuous tether was discretized into finite segments, with mass and forces concentrated at the tether nodes, which were connected by massless links. Coulombe-Pontbriand et al. [18] presents an experimental and numerical investigation of the dynamics of a tethered spherical helium balloon in outdoor conditions. Portable sensors were used to measure the balloon's motion, tether tension, and wind conditions. The measured data were then used to validate a 3D numerical model, in which the balloon is modeled as a rigid body subject to buoyancy, aerodynamic drag, and gravity, and attached to a tether represented by a lumped-mass model with internal stiffness and damping. The study highlights that the balloon's oscillations and surface roughness, combined with wind turbulence, result in a substantial increase in the drag coefficient. Aglietti [19] proposed a three-dimensional dynamic finite element model in commercial finite element (FE) software ANSYS in which aerodynamic loads are computed based on the relative velocity between a time-varying input airflow and the resulting structural velocities. The approach was applied to analyze the response of a tethered spherical aerostat to gusts, incorporating structural nonlinearity and capturing aspects of fluid-structure interaction between the aerostat and the tether. Unlike models using lumped masses connected by springs, beam elements in ANSYS were employed, allowing the inclusion of cable bending stiffness–which can be non-negligible in certain scenarios. Redi et al. [20] extended the finite element code to perform a comprehensive analysis of a lighter-than-air tethered platform operating under realistic design conditions. Their model accounts for gusts in all three spatial directions and includes simulations of continuous atmospheric turbulence. Beyond these classical studies, several works have specifically addressed the dynamic

control and parameter estimation of tethered systems in space applications. Smirnov et al. [21] and Malashin et al. [22] demonstrated that tether deployment in low Earth orbit is strongly influenced by longitudinal and transverse wave propagation, which significantly affects tension variations and end-mass dynamics, and validated their models against flight data from Young Engineers' Satellite 2 mission. Diakov et al. [23–25] extended these analyses to the control and parameter estimation of tethered systems for load transport and space debris removal, showing that system stability and performance critically depend on tether properties, payload mass, and deployment strategies. Collectively, these works emphasize that realistic dynamic modeling, including wave propagation and feedback control, is essential for the reliable design and operation of tethered space systems. In the present work, we adopt a quasi-static assumption for the tether, focusing on the interaction between the balloon and tether under lateral wind conditions. While this simplification neglects certain dynamic effects, it enables efficient capture of the primary behavior of the tethered balloon system and provides a practical framework for preliminary design and operational analysis. This assumption is justified under steady-wind conditions, as balloon tethers experience large, steady tensions due to lift and wind forces, which generally stabilize the system. Under such conditions, the quasi-static model accurately represents the main tension and configuration without requiring full dynamic analysis. However, in gusty or rapidly varying wind conditions, dynamic modeling becomes necessary to account for oscillations and transient effects.

*Study Rationale:* As reviewed above, while many studies have examined the ascent behavior and dynamic response of tethered aerostats, several important gaps remain in the literature. Addressing these gaps constitutes the primary motivation of the present study.

First, there is a lack of rigorous validation against analytical or high-fidelity numerical models. Validation against experimental data can be challenging, as factors such as wind gusts, balloon surface roughness, and other uncertainties–such as sensor inaccuracies, unsteady atmospheric conditions, and dynamic balloon oscillations–cannot be accurately controlled or measured. These issues often introduce significant discrepancies between experimental results and analytical predictions [26–28]. Therefore, an important step in model validation should include a direct comparison between discretized tether models and continuous cable finite element models. The former solves for the static equilibrium of the tether by applying force balance segment by segment, while the latter determines the tether shape by assembling the stiffness matrix and solving the system under prescribed boundary conditions. Despite the importance of such a comparison, it has rarely been addressed in the existing literature. Second, there is limited availability of open-source computational tools to enable rapid design iteration and community adoption. Most existing studies rely heavily on custom, author-developed codes, and there is a lack of openly available tools for the research community. This absence of shared resources [29,30] significantly limits the potential for rapid design iteration and collaborative development [31]. Third, there is a lack of inverse design capabilities that allow determining balloon and tether parameters for targeted operational requirements. Most existing models do not support inverse design–an essential feature for practical engineering applications. For example, under a given wind condition, one may need to determine the optimal balloon size or tether properties required to reach a specific altitude or achieve a desired horizontal drift to cover a targeted area. These tasks demand computational tools capable of both fast iterative analysis and inverse problem solving.

To address these limitations, this paper presents the analytical formulation of a tethered spherical balloon system under steady-state wind conditions. The model incorporates altitude-dependent atmospheric properties and systematically accounts for all external forces acting on the balloon and tether. The balloon is modeled as a rigid body with constant volume, subject to buoyancy, drag, and gravitational forces, and is connected to the ground via a long tether. The tether is discretized into multiple segments, and static equilibrium is established by balancing the aerodynamic drag, self-weight, and tension forces of each segment. The proposed method is implemented in a MATLAB-based simulation tool called the High-Altitude Tethered Aerostat Simulation (HATASIM) code, designed to predict the quasi-static ascent behavior of tethered spherical balloons. The tool enables rapid and accurate computation of balloon altitude, horizontal drift, tether shape, and tension distribution for a specified balloon size and tether length under varying wind conditions. To verify the accuracy of the HATASIM code, a finite element (FE) model was developed using continuous cable elements to represent the deformation of the tether. Excellent agreement was observed between the results of the HATASIM code and those from the in-house FE simulation. To further demonstrate its utility, parametric studies were conducted to evaluate the effects of balloon size, wind speed, and tether length on system behavior, including balloon altitude, lateral drift, tether configuration, and tension distribution. Notably, inverse design analysis can be efficiently performed using the pre-computed database, enabling the determination of the required balloon dimensions and tether length to achieve a specified deployment altitude and horizontal position. To support broader adoption and practical use, the HATASIM code has been made publicly available through a permanent GitHub repository https://github.com/SCU-AN-Group/HATASIM. It is worth noting that, although this work focuses on the ascent analysis of tethered spherical balloons, the developed method can be readily extended to model the ascent and dynamic response of tethered helikites or streamlined airships, provided that their aerodynamic characteristics are obtained through computational fluid dynamics or wind tunnel testing [7,32–34].

The remainder of this paper is organized as follows. Section 2 describes the atmospheric modeling assumptions. Section 3 presents the analytical formulation, outlines the solution algorithm, and details the MATLAB implementation of the simulation tool. Section 4 introduces the finite element formulation using continuous cable elements and provides a numerical example comparing the analytical results with high-fidelity FE simulations to verify the model's accuracy. Section 5 applies the method to investigate the effects of balloon size, tether length, and wind conditions on the ascent behavior of the tethered balloon. Finally, Section 6 summarizes the key findings and discusses potential directions for future research and development.

## 2. Atmospheric properties

The operational altitude of tethered balloons depends on the specific application, typically ranging from a few hundred meters to several kilometers, and is generally confined to the troposphere [11]. For modeling purposes, the atmospheric environment is assumed to be ideal, with meteorological factors such as humidity and suspended particulate matter neglected for simplicity.

### 2.1. Air temperature

According to the International Standard Atmosphere (ISA) model [35], within the troposphere, the temperature decreases by approximately 6.5 K for every 1000-meter increase in altitude. The atmospheric temperature as a function of altitude $h$ is given by:

$$T(h) = T_0 - 0.0065h \tag{1}$$

where $T_0$ is the reference temperature at sea level ($h = 0$), and is set to 288.15 K.

### 2.2. Air pressure

According to the ideal gas law and the hydrostatic equilibrium equation in the vertical direction of the atmosphere, the variation of air pressure with altitude can be derived as [35]:

$$P(h) = P_0\left(1 - 0.0065\frac{h}{T_0}\right)^{5.2561} \tag{2}$$

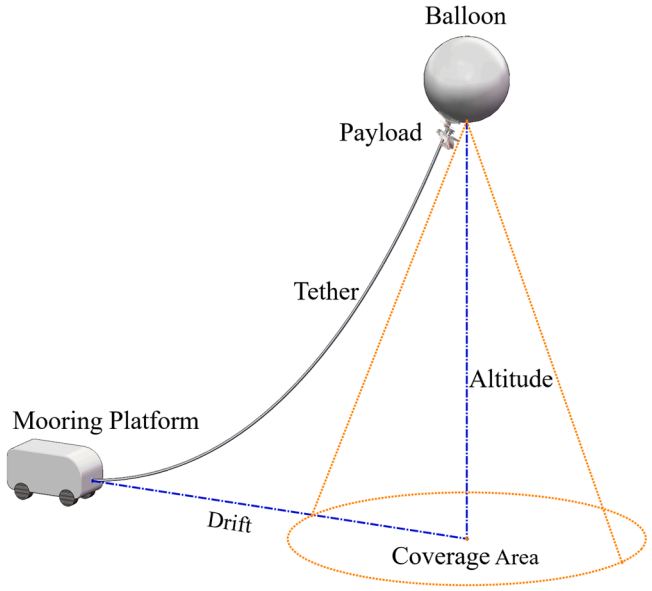


**Fig. 1.** Illustration of a typical operating configuration of a tethered balloon system, consisting of a vehicle-mounted mooring platform, a long tether, and a helium balloon that carries payloads.

where $P_0$ is the standard atmospheric pressure at sea level and is set to 101325 Pa.

### 2.3. Air density

Combining the expressions for air temperature and pressure with the ideal gas law, the variation of air density with altitude can be derived as:

$$\rho(h) = \rho_0 \left(1 - 0.0065 \frac{h}{T_0}\right)^{4.2561} \tag{3}$$

where $\rho_0$ is the air density at sea level and is set to 1.225 $\mathrm{kg/m^3}$.

### 2.4. Helium density

Helium is a commonly used lifting gas for tethered balloons. To maintain a constant envelope volume, a valve system is employed to regulate the amount of helium such that the internal helium pressure remains equal to the surrounding atmospheric pressure at all altitudes. Moreover, it is assumed that the balloon ascends slowly enough to remain in thermal equilibrium with the environment, implying that the temperature inside and outside the balloon is the same. Under these assumptions, and by applying the ideal gas law to helium in conjunction with the altitude-dependent atmospheric model, the expression for the helium density can be derived analogously to that of air density:

$$\rho_{\mathrm{He}}(h) = \frac{P_0 \left(1 - 0.0065 \frac{h}{T_0}\right)^{5.2561}}{R_{\mathrm{He}} \left(T_0 - 0.0065\ h\right)} \tag{4}$$

where $R_{\mathrm{He}}$ is the specific gas constant for helium is taken as $R_{\mathrm{He}} = 2077$ J/(kg·K).

### 2.5. Air viscosity

Sutherland's formula provides an approximation for how the dynamic viscosity of gases varies with temperature. Based on an idealized intermolecular force potential, the law is expressed as [36]:

$$\mu(h) = \mu_0 \left(\frac{T}{T_0}\right)^{1.5} \frac{T_0 + S}{T + S} \tag{5}$$

where $\mu(h)$ is the dynamic viscosity at altitude $h$, and $T$ is the atmospheric temperature at that altitude. $S$ is the Sutherland constant, an effective temperature characterizing the gas. For air, $S = 110.4$ K. The reference temperature is $T_0 = 288.15$ K, with the corresponding reference dynamic viscosity $\mu_0 = 1.79 \times 10^{-5}$ Pa · s.

### 2.6. Wind profile

The wind profile characterizes the variation of wind speed with altitude within the atmospheric boundary layer. The mean wind velocity $v(h)$ at height $h$ is modeled using a power law that represents the Earth's boundary layer:

$$v(h) = v_{\mathrm{ref}} \left(\frac{h}{h_{\mathrm{ref}}}\right)^{\alpha} \tag{6}$$

where $v_{\mathrm{ref}}$ is the reference wind speed at height $h_{\mathrm{ref}} = 10$ m, and $\alpha = 0.2$ is the power-law exponent commonly adopted for neutral atmospheric stability conditions, also known as the wind shear exponent. Fig. 2 shows the variation of wind speed $v(h)$ as a function of altitude $h$ for different reference wind speeds $v_{\mathrm{ref}}$, ranging from 1 m/s to 5 m/s.

## 3. Methodology

### 3.1. Balloon modeling

This study considers the most commonly used spherical helium balloon [37] as the object of investigation. The balloon is assumed to have a smooth surface and to maintain a constant volume during its ascent. Given that the ascent is sufficiently slow, the process is modeled as quasi-static, implying that the balloon remains in a state of static equilibrium at all times throughout the ascent [7]. The corresponding free-body diagram illustrating the force balance on the balloon is shown in Fig. 3.

Therefore, the static equilibrium of the balloon is governed by the balance of forces in both the vertical and horizontal directions, which can be expressed as:

$$\begin{cases} F_B - W_{\mathrm{bal}} - T\cos\theta = 0 \\ F_D - T\sin\theta = 0 \end{cases} \tag{7}$$

where $F_B$ is the buoyant force, $W_{\mathrm{bal}}$ is the total weight of the balloon and its payload, $F_D$ is the aerodynamic drag acting on the balloon, $T$ is the tension in the tether at the attachment point, and $\theta$ is the inclination angle of the tether relative to the vertical direction at the point of attachment. By solving Eq. 7, the tether tension $T$ and inclination angle $\theta$ at the balloon attachment point can be determined, provided that the buoyant force $F_B$, total weight $W_{\mathrm{bal}}$, and aerodynamic drag $F_D$ of the balloon are known. These quantities are all functions of the balloon's altitude and are defined in detail in the subsequent sections. The explicit solutions for the tether tension and inclination angle are:

$$\begin{cases} T = \dfrac{F_B - W_{\mathrm{bal}}}{\cos\theta} \\ \theta = \arctan\left(\dfrac{F_D}{F_B - W_{\mathrm{bal}}}\right) \end{cases} \tag{8}$$

#### 3.1.1. Weight

The total weight of the balloon consists of the weight of the balloon envelope, the payload, and the enclosed helium gas. It is expressed as:

$$W_{\mathrm{bal}}(h) = \left(m_{\mathrm{env}} + m_{\mathrm{load}} + \rho_{\mathrm{He}}(h)V\right)g \tag{9}$$

where:

- $m_{\mathrm{env}}$ is the mass of the balloon envelope,
- $m_{\mathrm{load}}$ is the mass of the payload,
- $\rho_{\mathrm{He}}(h)$ is the helium density at altitude $h$,
- $V = \frac{4}{3}\pi\left(\frac{D}{2}\right)^3$ is the constant volume of the spherical balloon, and $D$ denotes the diameter of the balloon,
- $g$ is the gravitational acceleration.

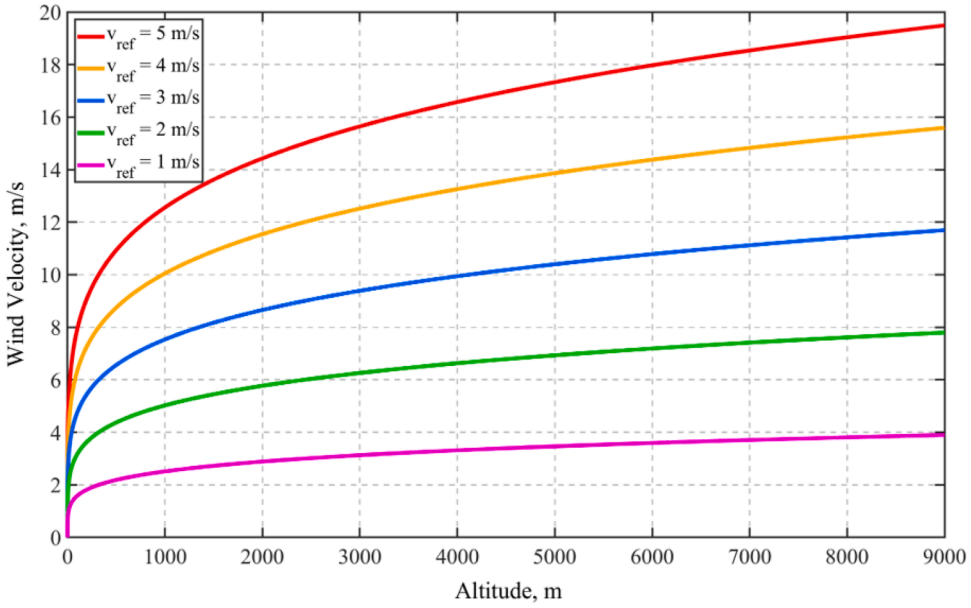


**Fig. 2.** Wind profile showing the variation of wind speed with altitude.

### 3.1.2. Buoyancy

Since the balloon considered in this study has a spherical shape, it does not generate any aerodynamic lift under wind. The vertical force acting on the balloon is solely due to static buoyancy, governed by Archimedes' principle. The buoyancy force at altitude $h$ is given by:

$$F_B(h) = \rho(h)\, g\, V \tag{10}$$

where:

- $\rho(h)$ is the ambient air density at altitude $h$,
- $V$ is the constant volume of the balloon,
- $g$ is the gravitational acceleration.

### 3.1.3. Aerodynamic drag

According to classical fluid mechanics [38], the aerodynamic drag force acting on a spherical tethered balloon can be expressed as:

$$F_D(h) = \frac{1}{2}\,\rho(h)\, v^2(h)\, A_{\text{bal}}\, C_D, \tag{11}$$

where:

- $\rho(h)$ is the air density at altitude $h$,
- $v(h)$ is the horizontal wind velocity at altitude $h$,
- $A_{\text{bal}} = \pi D^2/4$ is the projected frontal area of the balloon,
- $C_D$ is the drag coefficient, which depends on the Reynolds number of the balloon $Re_{\text{D}}$.

The drag coefficient $C_D$ for a smooth sphere exhibits a strong nonlinear dependence on the Reynolds number $Re_{\text{D}}$ [39–41]. At very low Reynolds numbers ($Re_{\text{D}} \le 1$), the flow is dominated by viscous forces (creeping flow), and $C_D$ follows Stokes' law. As $Re_{\text{D}}$ increases ($1 < Re_{\text{D}} \le 10^3$), inertial effects become significant, and the Schiller-Naumann correction provides an improved estimate . In the intermediate regime ($10^3 < Re_{\text{D}} \le 2\times10^5$), $C_D$ stabilizes around 0.47. Beyond the critical Reynolds number ($Re_{\text{D}} > 2\times10^5$), a drag crisis occurs due to the early transition of the boundary layer to turbulence, leading to a sharp drop in $C_D$ to about 0.2. This behavior is captured by the following piecewise expression:

$$C_D(Re_{\text{D}}) = \begin{cases} \dfrac{24}{Re_{\text{D}}}, & 0 < Re_{\text{D}} \le 1 \\ \dfrac{24}{Re_{\text{D}}}\left(1 + 0.15\, Re_{\text{D}}^{0.687}\right), & 1 < Re_{\text{D}} \le 10^3 \\ 0.47, & 10^3 < Re_{\text{D}} \le 2\times10^5 \\ 0.2, & Re_{\text{D}} > 2\times10^5 \end{cases} \tag{12}$$

The Reynolds number of the balloon at altitude $h$ is given by:

$$Re_{\text{D}}(h) = \frac{\rho(h)\, v(h)\, D}{\mu(h)}, \tag{13}$$

where $\mu(h)$ is the dynamic viscosity of air at altitude $h$.

### 3.2. Tether modeling

The tether is modeled as a flexible, homogeneous cylindrical rope. By gradually releasing it through controlled winch operation, a quasi-static and stable ascent of the balloon is achieved. During this process, the tether is considered to have one end anchored to the ground and the other end pulled upward by the balloon, while the entire tether is subjected to wind-induced aerodynamic forces. The released tether length increases incrementally, maintaining equilibrium at each step.

As illustrated in Fig. 4a, the tether is discretized into a finite number of straight, uniform segments, labeled sequentially from 1 to $n$, starting at the top (connected to the balloon) and extending down to the ground anchor. Each segment connects two adjacent nodes; specifically, the $i$-th segment spans from node $i$ to node $i+1$, with its center height denoted as $h_i$ and its inclination angle $\theta_i$ measured relative to the vertical axis. The free-body diagram of the $i$-th segment is shown in Fig. 4b. This segment is subjected to the following forces: its self-weight $m_i g$, the aerodynamic force $D_i$, and the tension forces at its two ends, denoted as $T_i$ (at the upper node) and $T_{i+1}$ (at the lower node). The aerodynamic force $D_i$ can be decomposed into two orthogonal components: a tangential component $D_{\tau i}$, acting along the segment direction, and a normal component $D_{ni}$, acting perpendicular to the segment. It is assumed that the tension force $T_i$ is aligned with the inclination angle $\theta_i$ of the $i$-th segment, while $T_{i+1}$ is aligned with the inclination angle $\theta_{i+1}$ of the $(i+1)$-th segment.

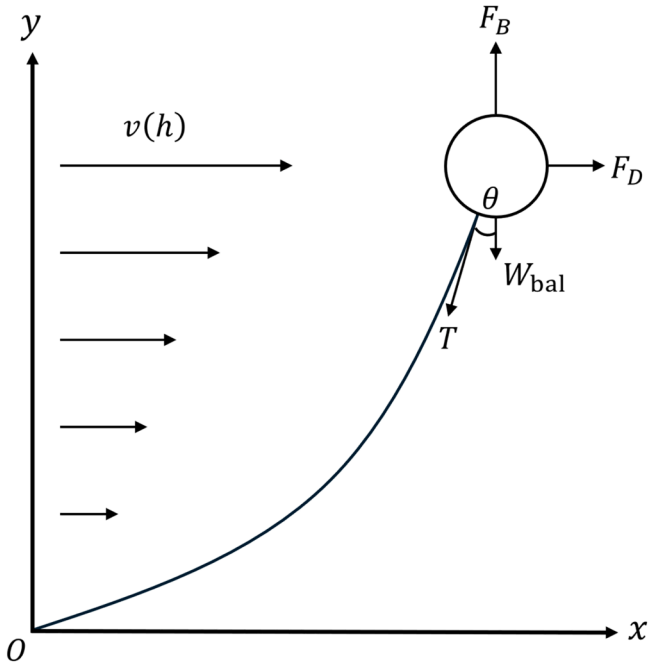


**Fig. 3.** Free-body diagram of the tethered balloon.

By enforcing static equilibrium in both the horizontal and vertical directions at the center of each segment, the following equations are obtained:

$$\begin{cases} T_i \sin\theta_i - T_{i+1}\sin\theta_{i+1} + D_{\tau i}\sin\theta_i + D_{ni}\cos\theta_i = 0 \\ T_i \cos\theta_i - T_{i+1}\cos\theta_{i+1} - m_i g + D_{\tau i}\cos\theta_i - D_{ni}\sin\theta_i = 0 \end{cases} \tag{14}$$

It should be noted that the segment weight $m_i g$ is a function of the segment length, and the aerodynamic force $D_i$ is a function of the altitude of the segment. Their expressions will be introduced in subsequent subsections. Given the tension force $T_i$ and inclination angle $\theta_i$ at node $i$, the equilibrium equations above can be used recursively to determine the tension force $T_{i+1}$ and inclination angle $\theta_{i+1}$ at the next node:

$$\begin{cases} \theta_{i+1} = \arctan\left(\dfrac{T_i \sin\theta_i + D_{\tau i}\sin\theta_i + D_{ni}\cos\theta_i}{T_i\cos\theta_i + D_{\tau i}\cos\theta_i - D_{ni}\sin\theta_i - m_i g}\right) \\ T_{i+1} = \dfrac{T_i\sin\theta_i + D_{\tau i}\sin\theta_i + D_{ni}\cos\theta_i}{\sin\theta_{i+1}} \end{cases} \tag{15}$$

Since the tension force $T_1$ and inclination angle $\theta_1$ at the top node (node 1 attached to the balloon) can be obtained by solving the static equilibrium of the balloon, as provided in Eq. 8. Therefore, by iteratively solving Eq. 15, the tension force and inclination angle of each segment can be sequentially determined along the tether.

#### 3.2.1. Segment mass

To discretize the tether and ensure the accuracy of the results, each segment is assigned a sufficiently small characteristic length, denoted by $K$. The total deployed tether length $L$ is then given by:

$$L = Kn, \tag{16}$$

where $n$ is the total number of discretized segments.

The mass of each segment can then be expressed as:

$$m_i = \rho_{\text{tet}} A_{\text{tet}} K, \tag{17}$$

where $\rho_{\text{tet}}$ is the density of the tether material, $A_{\text{tet}} = \frac{1}{4}\pi d^2$ is the cross-sectional area of the tether, and $d$ denotes the diameter of the tether's circular cross-section.

#### 3.2.2. Aerodynamic drag

Each tether segment is subjected to wind, which induces aerodynamic drag forces $D_i$. These forces are evaluated at the center of the segment, located at altitude $h_i$. The total drag force is decomposed into two components: a tangential component $D_{\tau i}$, corresponding to flow along the axial direction of the segment (i.e., along the cylinder), and a normal component $D_{ni}$, corresponding to flow perpendicular to the segment (i.e., around the cylinder). These components are expressed as:

$$\begin{cases} D_{\tau i}(h_i) = \dfrac{1}{2}\rho(h_i)\, v^2(h_i)\, \sin^2\theta_i\, A_i\, C_{d\tau i} \\ D_{ni}(h_i) = \dfrac{1}{2}\rho(h_i)\, v^2(h_i)\, \cos^2\theta_i \sqrt{\dfrac{4A_i}{\pi}}\,(K + \Delta L_i)\, C_{dni} \end{cases} \tag{18}$$

where $A_i$ is the deformed cross-sectional area of the segment, assuming volume conservation, and is given by:

$$A_i = \frac{A_{\text{tet}} K}{K + \Delta L_i} \tag{19}$$

The elongation $\Delta L_i$ of the segment is computed using Hooke's law:

$$\Delta L_i = \frac{T_i K}{E A_{\text{tet}}} \tag{20}$$

Here, $E$ is the Young's modulus of the tether, and $A_{\text{tet}}$ is the initial (undeformed) cross-sectional area of the tether.

It should be noted that the drag coefficient $C_{d\tau i}$ can be approximated by the frictional drag coefficient of a flat plate, while $C_{dni}$ corresponds to the pressure drag coefficient of a circular cylinder, as the flow perpendicular to the tether direction resembles crossflow over a cylinder. Calculations indicate that $C_{dni}$ is typically two orders of magnitude greater than $C_{d\tau i}$; hence, the contribution of the axial drag component $D_{\tau i}$ can be neglected in subsequent analyses.

The drag coefficient $C_{dni}$ is modeled as a piecewise function of the Reynolds number of the tether segment $Re_{di}$, following the formulation in [41,42]:

$$C_{dni}(Re_{di}) = \begin{cases} \dfrac{8\pi}{Re_{di}(2 - \ln Re_{di})}, & 0 < Re_{di} \le 1 \\ 1 + \dfrac{10}{Re_{di}^{2/3}}, & 1 < Re_{di} \le 10^2 \\ 1.2, & 10^2 < Re_{di} \le 2\times 10^5 \\ 0.3, & Re_{di} > 2\times 10^5 \end{cases} \tag{21}$$

The Reynolds number for the segment is defined as:

$$Re_{di}(h) = \frac{\rho(h) v(h) \cos\theta_i \sqrt{\dfrac{4A_i}{\pi}}}{\mu(h)} \tag{22}$$

### 3.3. Numerical implementation

For a given balloon tethered with a specified cable, and assuming that all relevant parameters–including wind conditions, balloon geometry, and tether properties–are known, the ascent process is simulated by incrementally increasing the balloon's altitude. At each altitude step, the corresponding horizontal drift of the balloon, as well as the tether's shape and tension distribution, are computed using the governing equations described in the previous sections. The simulation method proceeds as follows.

Let $H$ denote the height of the center of the balloon, and $h_i$ the height of the center of the $i$-th tether segment. The height $h_i$ is computed recursively as:

$$h_i = H - \frac{1}{2}D - \sum_{j=1}^{i}\left(K + \Delta L_j\right)\cos\theta_j + \frac{1}{2}\left(K + \Delta L_i\right)\cos\theta_i \tag{23}$$

where $i = 1, 2, \ldots, n$. $\Delta L_j$ is the elongation of the $j$-th segment, and $\theta_j$ is its inclination angle with respect to the vertical. In the analysis, the

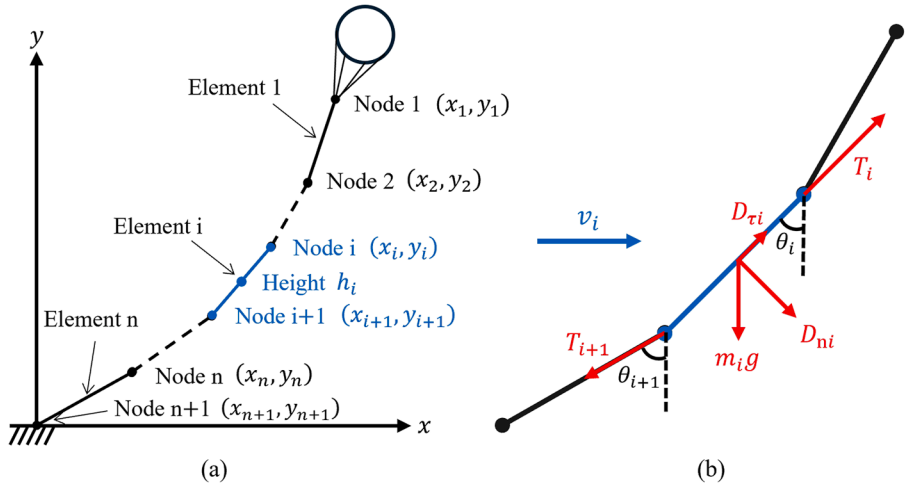


**Fig. 4.** Tether modeling. (a) Discretization of the tether, (b) Free-body diagram of a tether segment.

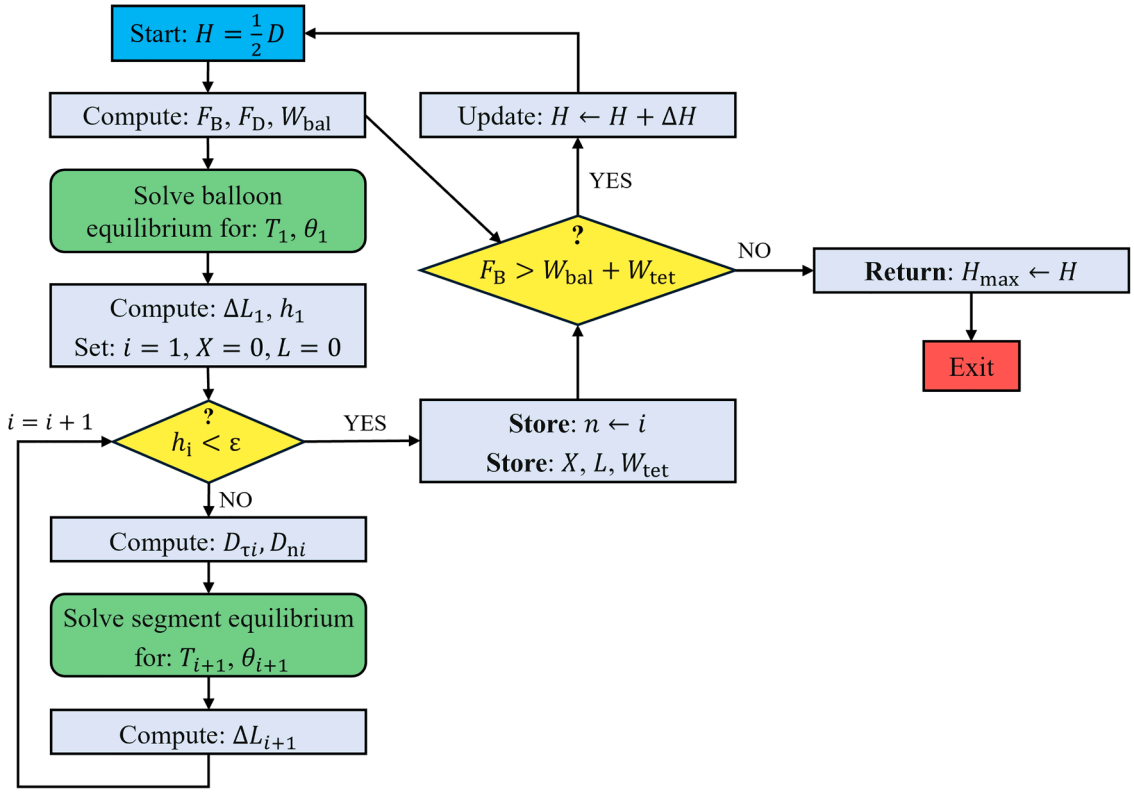


**Fig. 5.** Flowchart illustrating the computational procedure for simulating the quasi-static ascent of a tethered balloon system.

segment length $K$ is set to a sufficiently small fixed value to ensure numerical accuracy, for example $K = 0.1$ m.

Given the balloon altitude $H$, the force balance on the balloon can be solved using Eq. 8 to determine the tether tension $T_1$ and inclination angle $\theta_1$ at Node 1. Then, the elongation $\Delta L_1$ of the first segment is calculated, followed by its center height $h_1$ using Eq. 23. Using the force balance equations for the first segment (Eq. 15), the tension $T_2$ and inclination angle $\theta_2$ at the second node are determined. This process is repeated iteratively until the altitude of the final segment satisfies the condition

$$h_n < \varepsilon \tag{24}$$

where $\varepsilon$ is a small threshold tolerance, e.g., 0.001 m. Eq. 24 indicates that the $n$−th segment has effectively reached ground level. Once the total number of segments $n$ is determined, the total deployed tether length $L$ and horizontal drift $X$ of the balloon can be computed as:

$$\begin{cases} L = nK, \\ X = \sum_{i=1}^{n} \left(K + \Delta L_i\right) \sin\theta_i, \end{cases} \tag{25}$$

After computing the system at a given altitude H, the altitude is incremented by a step ΔH to calculate the system at the next altitude level. It is also important to note that the maximum balloon altitude $H_{max}$ must remain below a critical threshold, beyond which the total weight of the balloon and the deployed tether would exceed the available buoyant force. In other words, the following inequality must be satisfied at all

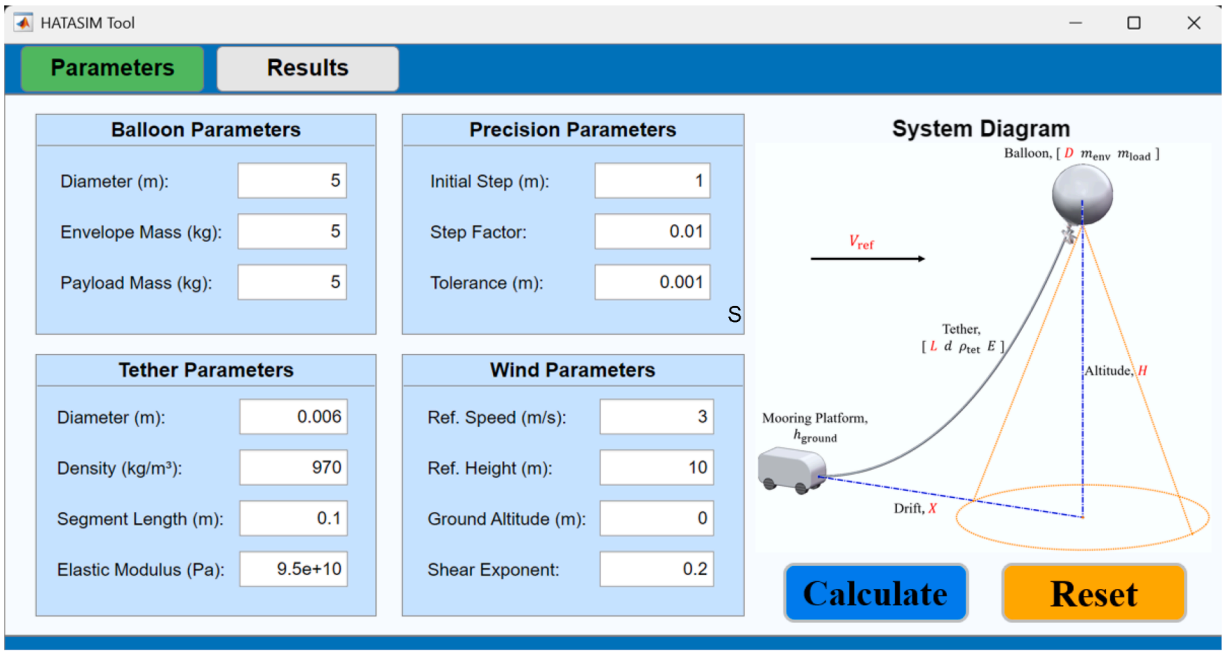


(a)


(b)

**Fig. 6.** Graphical user interface of HATASIM. (a) Input parameters. (b) Output results.

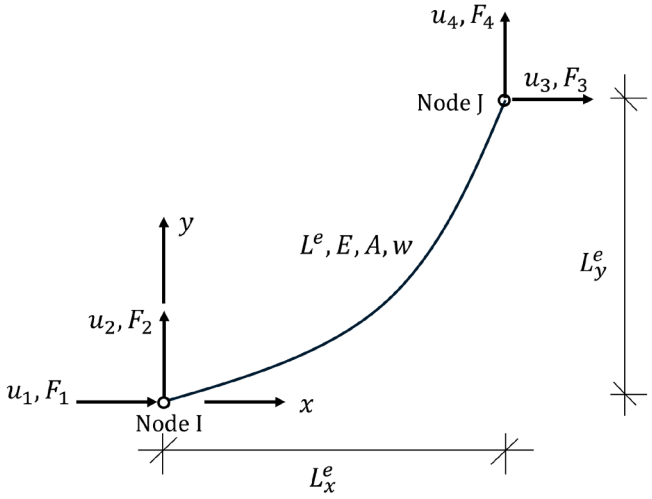


**Fig. 7.** Finite element representation of a catenary cable.

times during the ascent:

$$W_{\text{bal}} + W_{\text{tet}} < F_B(H), \tag{26}$$

where $W_{\text{bal}}$ is the total weight of the balloon and payload, and $W_{\text{tet}} = \rho_{\text{tet}} A_{\text{tet}} L g$ is the weight of the deployed tether of length $L$, with $\rho_{\text{tet}}$ denoting the material density, $A_{\text{tet}}$ the cross-sectional area, and $g$ the gravitational acceleration. $F_B(H)$ is the buoyant force at altitude $H$, as defined in Eq. 10. This condition ensures that the system remains in quasi-static equilibrium and that the balloon can sustain the load. In numerical practice, when Eq. 26 is not satisfied, the altitude increment ΔH is multiplied by a small factor, called the step factor (e.g., 0.01), to update the altitude. This procedure is repeated until the condition is satisfied, allowing a more accurate determination of the maximum altitude the system can reach.

The solution procedure is summarized in the flowchart shown in Fig. 5 and detailed in Algorithm 1. This algorithm has been implemented in MATLAB R2023b to perform the simulation. To facilitate application of the method, a graphical user interface (GUI) called the High-Altitude Tethered Aerostat Simulation tool (HATASIM) was developed (Fig. 6). In the "Parameters" interface (Fig. 6a), users enter the required inputs for the balloon, tether, wind, and calculation precision, then press the "Results" button. The left panel displays the ascent path and final tether shape, while the right panel shows the tether tension distribution, as shown in Fig. 6b. The query text function can then be used to calculate the altitude, drift, and tether shape at a prescribed released tether length, as well as the maximum tether tension at the balloon-tether interface for safety checks.

**Algorithm 1** Tethered balloon ascent simulation.

**Require:** Balloon altitude $H$, balloon properties $(D, W_{\text{bal}})$, tether segment length $K$, tether properties $(\rho_{\text{tet}}, E, A_{\text{tet}})$, wind model $(\rho(h), v(h), \mu(h))$, ascent step $\Delta H$, ground threshold $\varepsilon$
**Ensure:** Horizontal drift $X$, total tether length $L$ at any balloon altitude $H$, and maximum balloon altitude $H_{\max}$

$H \leftarrow \frac{1}{2}D$ ▷ Balloon initially on the ground
**while** True **do**
  Compute buoyant force $F_B(H)$
  Estimate balloon weight: $W_{\text{bal}} \leftarrow W_{\text{env}} + W_{\text{He}} + W_{\text{load}}$
  Estimate deployed tether weight: $W_{\text{tet}} \leftarrow \rho_{\text{tet}} \cdot A_{\text{tet}} \cdot L$
  **if** $F_B(H) \le W_{\text{bal}} + W_{\text{tet}}$ **then**
    **break** ▷ Buoyancy insufficient for further ascent
  **end if**
  Compute balloon drag force $F_D(H)$
  Solve balloon equilibrium to obtain $T_1$ and $\theta_1$
  Compute elongation: $\Delta L_1 \leftarrow \frac{T_1 K}{E A_{\text{tet}}}$
  Compute center height of first segment: $h_1 \leftarrow H - \frac{1}{2}D - \frac{1}{2}(K + \Delta L_1)\cos\theta_1$
  Initialize $i \leftarrow 1$, $L \leftarrow 0$, $X \leftarrow 0$
  **while** $h_i > \varepsilon$ **do**
    Compute aerodynamic forces $D_{ri}$ and $D_{ni}$ at $h_i$
    Solve segment equilibrium to get $T_{i+1}$ and $\theta_{i+1}$
    Compute elongation: $\Delta L_{i+1} \leftarrow \frac{T_{i+1} K}{E A_{\text{tet}}}$
    Compute center height: $h_{i+1} \leftarrow h_i - \frac{1}{2}(K + \Delta L_{i+1})\cos\theta_{i+1}$
    $i \leftarrow i + 1$
  **end while**
  Store $n \leftarrow i$ ▷ Number of tether segments from $H$ to ground
  Compute total drift: $X \leftarrow \sum_{j=1}^{n}(K + \Delta L_j)\sin\theta_j$
  Compute total tether length (undeformed): $L \leftarrow K \cdot n$
  Compute total tether length (deformed): $l \leftarrow L + \sum_{j=1}^{n}\Delta L_j$
  Update balloon altitude: $H \leftarrow H + \Delta h$
**end while**
**return** $X$, $L$ at any given $H$, and $H_{\max} \leftarrow H$

## 4. Method verification

In this section, we present a representative numerical example to demonstrate the effectiveness of the proposed method in predicting the ascent behavior of a tethered spherical balloon, and validate its accuracy by developing a finite element (FE) code for comparison.

### 4.1. Finite element method

To verify the accuracy of the proposed analytical method, we developed a finite element (FE) code specifically tailored for cable structures. This FE procedure computes the deformed shape and tension distribution of the tether based on a prescribed unstressed tether length, boundary conditions (including fixed and loaded ends), and distributed aerodynamic loads. The resulting numerical solution serves as a reference for validating the quasi-static equilibrium configuration and internal force distribution obtained from the analytical method.

In the FE analysis, the tether is discretized into multiple two-node curved cable elements. Consider an elastic catenary cable element stretched in the vertical plane, with unstressed elemental length $L^e$, Young's modulus $E$, cross-sectional area $A$, and weight per unit length $w$, as illustrated in Fig. 7. Assuming that the cable is perfectly flexible (i.e., incapable of resisting bending or compression) and that Hooke's law governs the material behavior, the exact relationships between the horizontal and vertical projections of the element and the internal force components at its ends, as well as the deformed cable length relative to the initial unstressed length, are given by Pevrot and Goulois [43]:

$$L_x^e = -F_1\left[\frac{L}{EA} + \frac{1}{w}\ln\left(\frac{F_4 + T_J}{T_I - F_2}\right)\right], \tag{27}$$

$$L_y^e = \frac{1}{2EAw}(T_J^2 - T_I^2) + \frac{T_J - T_I}{w}, \tag{28}$$

$$L_{\text{def}}^e = L^e + \frac{1}{2EAw}\left(F_4 T_J + F_2 T_I + F_1^2 \ln\left(\frac{F_4 + T_J}{T_I - F_2}\right)\right), \tag{29}$$

where $L_x^e$ and $L_y^e$ are the horizontal and vertical projections of the cable element, respectively. $F_1$ and $F_2$ are the horizontal and vertical force components at node $I$, and $F_3$ and $F_4$ are those at node $J$. $T_I$ and $T_J$ are the tension magnitudes at nodes $I$ and $J$, respectively. These quantities are related through the following expressions:

$$\begin{aligned} F_3 &= -F_1, & F_4 &= -F_2 + wL, \\ T_I &= \sqrt{F_1^2 + F_2^2}, & T_J &= \sqrt{F_3^2 + F_4^2}. \end{aligned} \tag{30}$$

Therefore, only two force variables, namely $F_1$ and $F_2$, are independent.

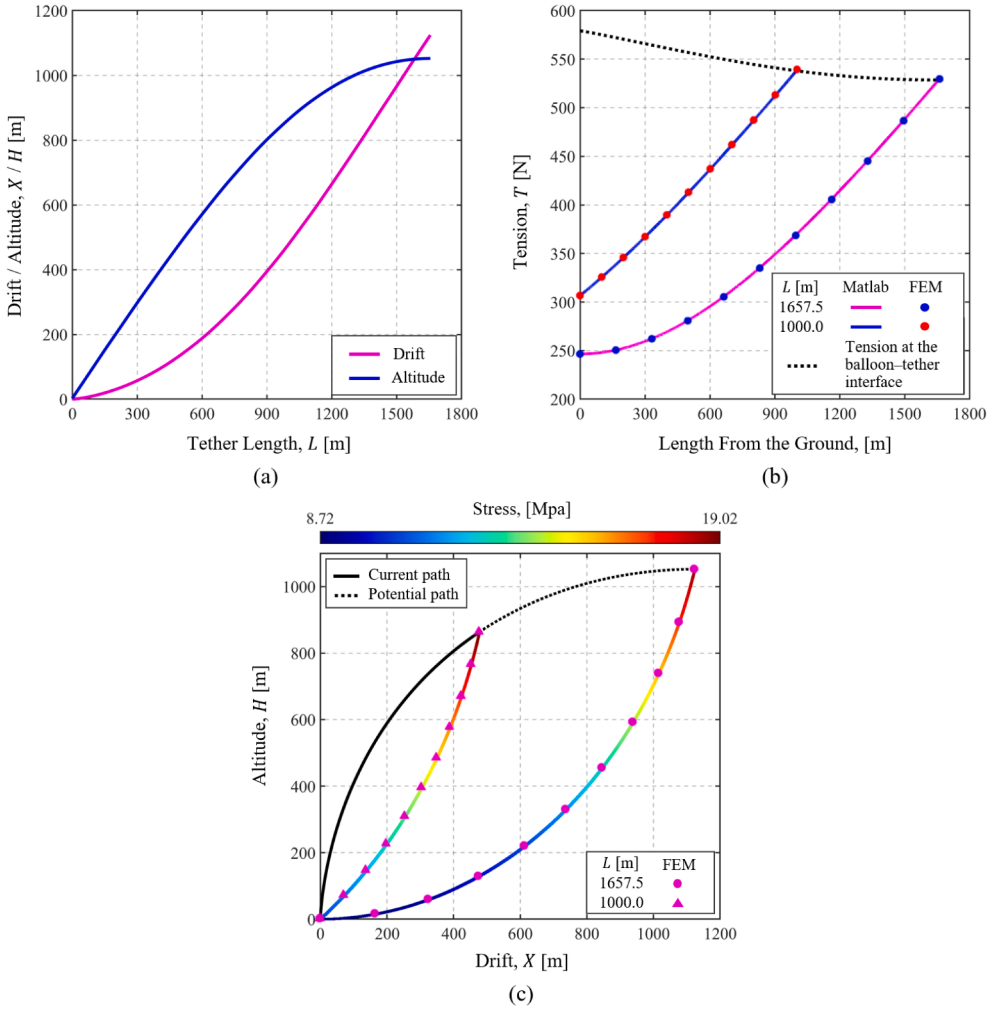


**Fig. 8.** Predicted ascent path of a tethered balloon with a diameter of 5 m under a reference wind speed of 3 m/s. (a) Evolution of the balloon's horizontal drift and altitude as the tether length increases. (b) Tension force distribution along the tether. (c) Ascent path of the balloon and corresponding tether profile, color-coded by tension stress.

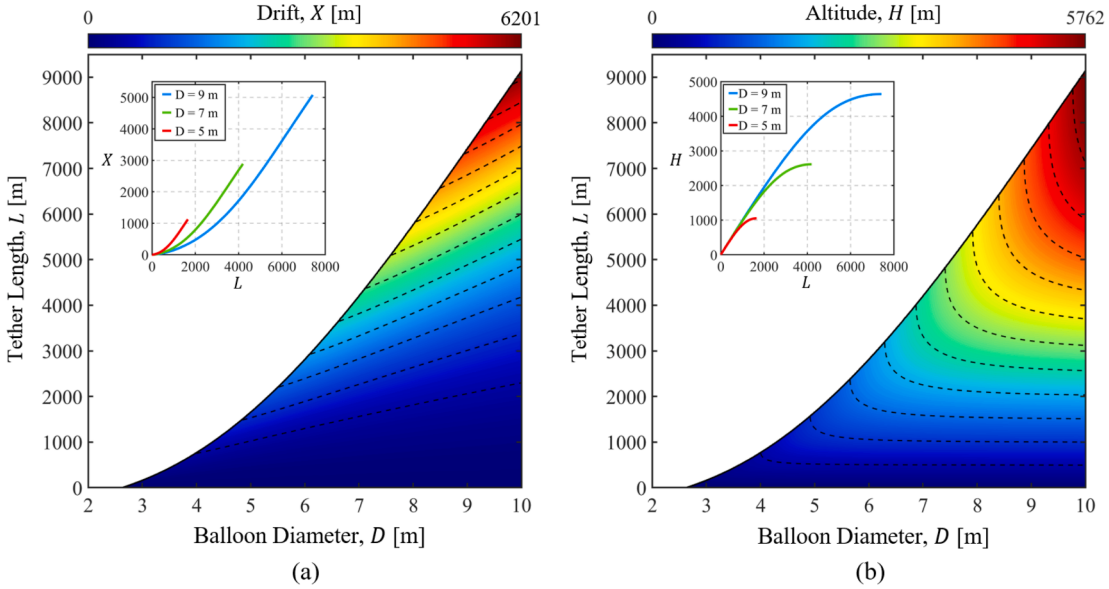


**Fig. 9.** Variations of (a) horizontal drift $X$ and (b) altitude $H$ of the tethered balloon as functions of the balloon diameter $D$ and tether length $L$ under a specified wind condition of 3 m/s. The insets in (a) and (b) illustrate the variatins of $X$ and $H$ for three specific balloon diameters of 5, 7, and 9 m, respectively.

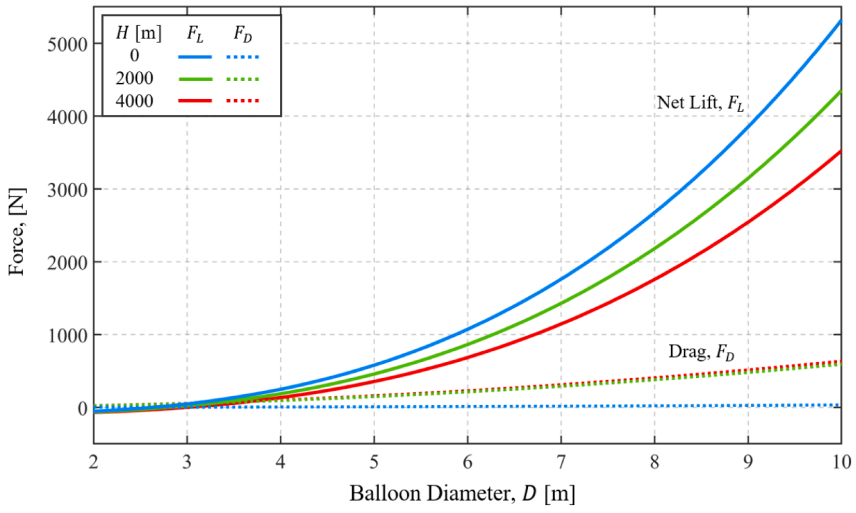


**Fig. 10.** Variation of the net lift, $F_L = F_B - W_{\text{bal}}$, and aerodynamic drag, $F_D$, acting on the balloon as a function of balloon diameter $D$.

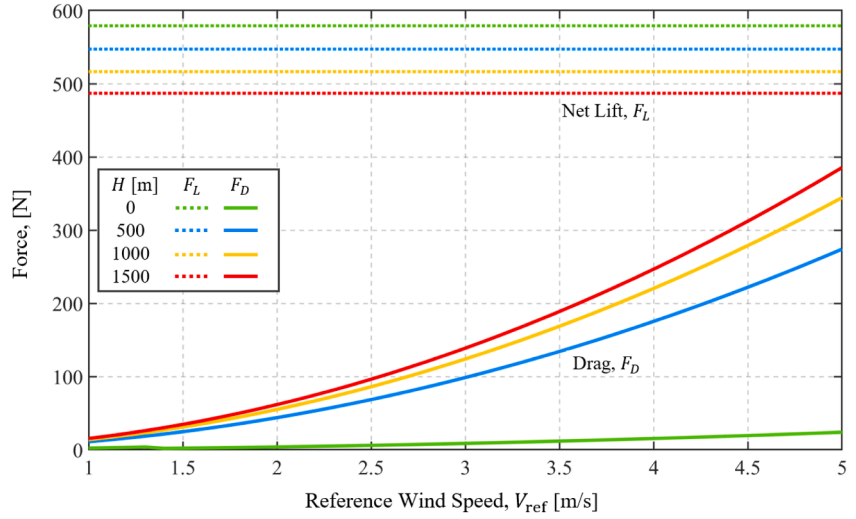


**Fig. 11.** Variation of the net lift, $F_L = F_B - W_{\text{bal}}$, and aerodynamic drag, $F_D$, acting on the balloon as a function of the reference wind speed $v_{\text{ref}}$.

The element length projections $L_x^e$ and $L_y^e$ are written as functions of the nodal forces at node $I$:

$$L_x^e = L_x^e(F_1, F_2), \quad L_y^e = L_y^e(F_1, F_2). \tag{31}$$

Differentiating $L_x^e$ and $L_y^e$ with respect to the nodal forces $F_1$ and $F_2$, and arranging the results in matrix form yields:

$$\begin{bmatrix} dL_x \\ dL_y \end{bmatrix} = \begin{bmatrix} \dfrac{\partial L_x^e}{\partial F_1} & \dfrac{\partial L_x^e}{\partial F_2} \\ \dfrac{\partial L_y^e}{\partial F_1} & \dfrac{\partial L_y^e}{\partial F_2} \end{bmatrix} \begin{bmatrix} dF_1 \\ dF_2 \end{bmatrix} = \mathbf{F} \begin{bmatrix} dF_1 \\ dF_2 \end{bmatrix}, \tag{32}$$

where $\mathbf{F}$ is the *incremental flexibility matrix*. The *tangent stiffness matrix* $\mathbf{K}$ is defined as the inverse of $\mathbf{F}$:

$$\mathbf{K} = \mathbf{F}^{-1} = \begin{bmatrix} k_1 & k_2 \\ k_3 & k_4 \end{bmatrix} \tag{33}$$

Noting that $k_2 = k_3$, the tangent stiffness matrix $\mathbf{K}_t$ in terms of the four nodal degrees of freedom is given by:

$$\mathbf{K}_t = \begin{bmatrix} -k_1 & -k_2 & k_1 & k_2 \\ -k_2 & -k_4 & k_2 & k_4 \\ k_1 & k_2 & -k_1 & -k_2 \\ k_2 & k_4 & -k_2 & -k_4 \end{bmatrix}. \tag{34}$$

The tangent stiffness matrix $\mathbf{K}_t$ relates the incremental element nodal force vector $\Delta\mathbf{f} = [\Delta F_1\ \Delta F_2\ \Delta F_3\ \Delta F_4]^T$ to the corresponding incremental nodal displacement vector $\Delta\mathbf{u} = [\Delta u_1\ \Delta u_2\ \Delta u_3\ \Delta u_4]^T$. Symbolic computation in MATLAB was used to evaluate the required partial derivatives and construct the stiffness matrix. It can be seen that $\mathbf{K}_t$ depends on the current internal force components $F_1$, $F_2$, or the current geometry $L_x$, $L_y$, it inherently captures the geometric nonlinearity of the system. It should be noted that the cable element typically exhibits negligible stiffness in its unstressed state. To initiate deformation calculations under external loads, an initial stiffness is introduced by pre-stressing the cable via its self-weight. Specifically, $F_1$ and $F_2$ are initialized based on the deformation induced by gravity using the following well-known catenary approximations:

$$F_1^0 = -\frac{wL_x^e}{2\lambda}, \tag{35}$$

$$F_2^0 = \frac{w}{2}\left(-L_y^e \frac{\cosh(\lambda)}{\sinh(\lambda)} + L^e\right), \tag{36}$$

where $\lambda > 0$ is a shape parameter determined by solving:

$$(L^e)^2 = (L_y^e)^2 + (L_x^e)^2 \frac{\sinh^2(\lambda)}{\lambda^2}. \tag{37}$$

Eqs. (35)–(36) provide initial estimates for $F_1$ and $F_2$ from the undeformed geometry and self-weight. However, to account for cable stretch

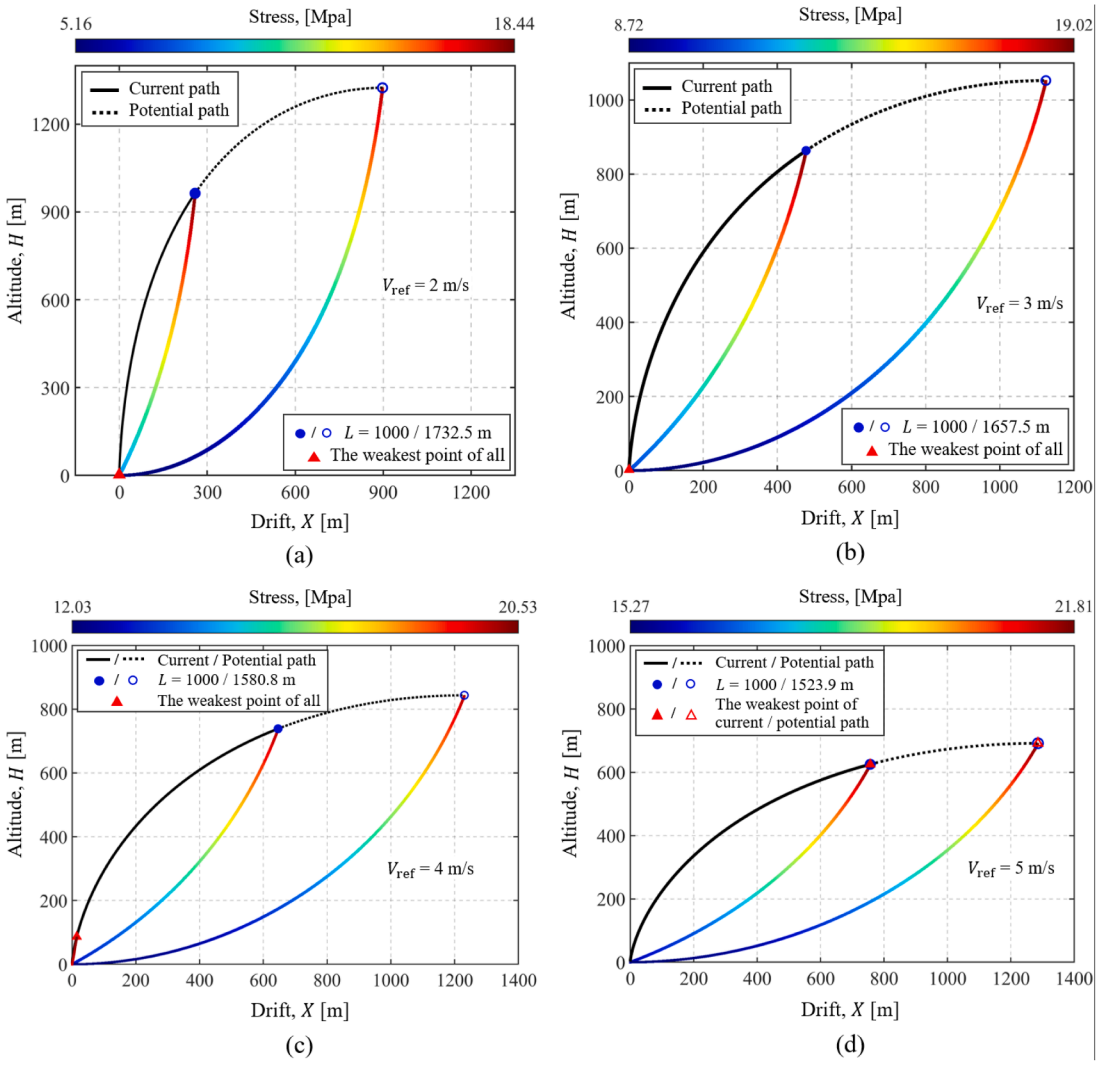


**Fig. 12.** Ascent path and intermediate tether shape with tension distribution for the balloon of 5 m diameter. (a) $v_{ref}$ = 2 m/s. (b) $v_{ref}$ = 3 m/s. (c) $v_{ref}$ = 4 m/s. (d) $v_{ref}$ = 5 m/s.

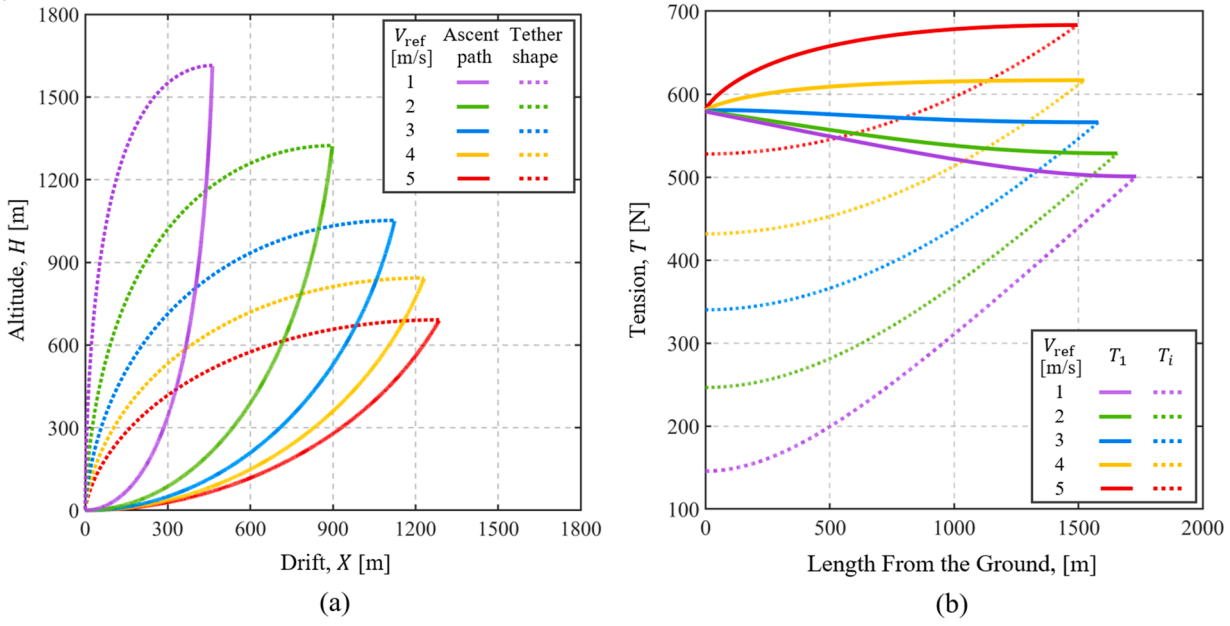


**Fig. 13.** Effect of wind speed on the ascent behavior of the tethered balloon system. (a) Balloon ascent path and tether profile under various wind speeds. (b) Maximum tether tension and tension distribution along the tether at different wind speeds.

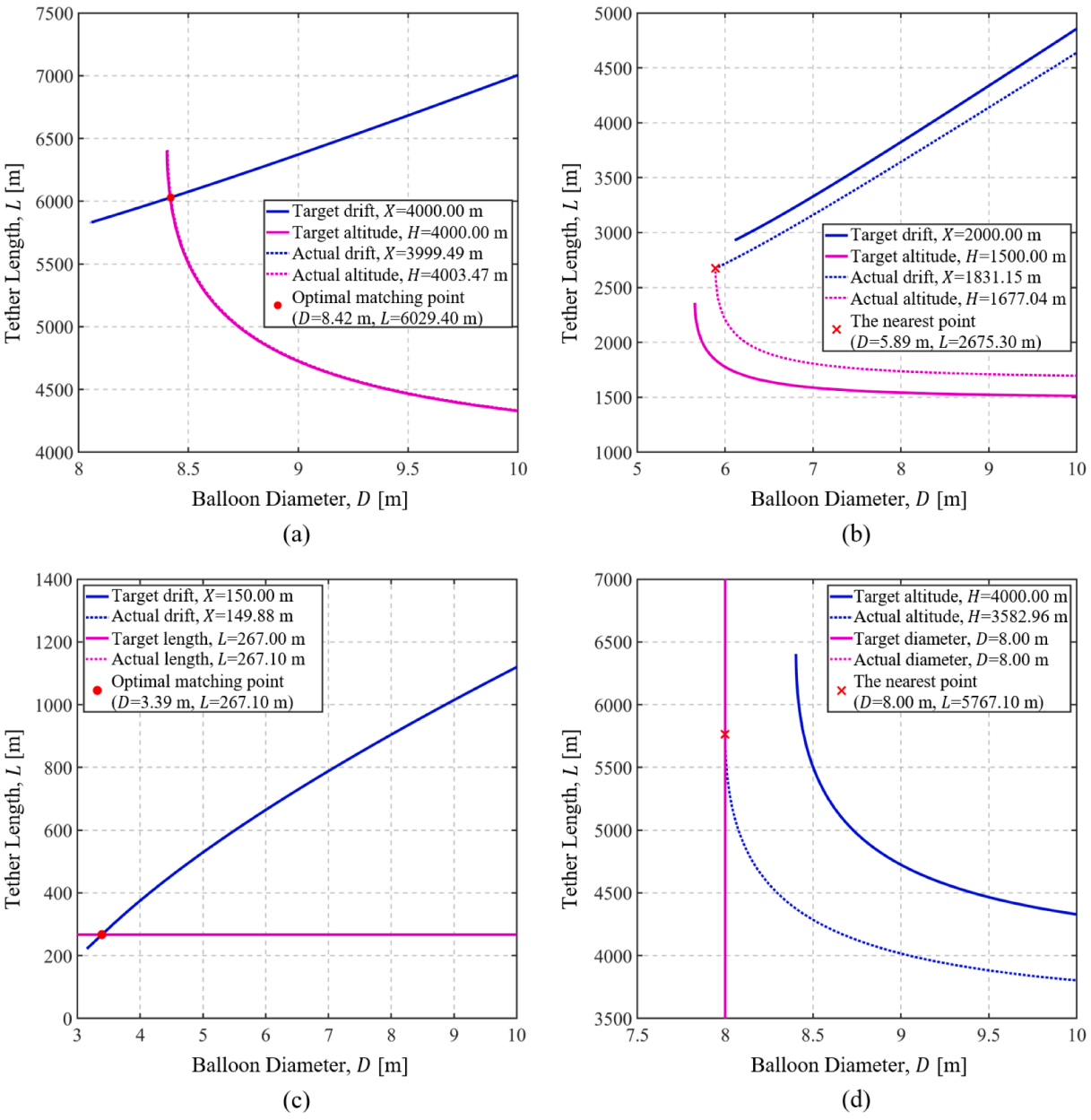


**Fig. 14.** Inverse design demonstration examples. (a) Given a target drift and altitude, the corresponding balloon diameter and tether length are determined. (b) When the specified design cannot be achieved, the nearest feasible design point is provided. (c) For a specified tether length, the balloon diameter is determined to achieve a target drift. (d) For a given balloon size, the required tether length is determined to reach a target altitude.

due to internal tension, an iterative procedure is required to refine these estimates such that they satisfy the nonlinear force-displacement relations in Eqs. (27)–(29). This procedure is well-documented in the literature [43] and omitted here for brevity.

Once the tangent stiffness matrix of the cable element is obtained, the deformation analysis of the tether proceeds by assembling the elemental stiffness matrices into a global stiffness matrix. Since the catenary cable element is inherently curved, the tether can be discretized using significantly fewer cable elements compared to the number of segments required in the force-balance analytical method described earlier. Appropriate boundary conditions are applied, including fixing the bottom end of the tether to the ground and applying the resultant force from the balloon's static equilibrium to the top end. Total aerodynamic loads acting on each cable element are computed and converted into equivalent nodal forces. The global nonlinear equilibrium equations are then solved using the Newton-Raphson iterative method. This standard nonlinear finite element procedure is well-documented in textbooks and is therefore not repeated here. The developed nonlinear FEM code has been implemented in MATLAB R2023B and will be made publicly available via GitHub for academic use: https://github.com/SCU-AN-Group/HATASIM.

### 4.2. Numerical example

To be specific, yet without loss of generality, the balloon in this example is assumed to have a diameter of 5 m, and the total mass of the balloon envelope and payload is set to 10 kg. The tether is modeled as ultra-high-molecular-weight polyethylene (UHMWPE), with a density of 970 kg/m$^3$, an elastic modulus of 95 GPa, and a circular cross-section with a diameter of 6 mm. The ascent of the balloon is simulated under a reference wind speed of 3 m/s measured at sea level. The key physical and simulation parameters are summarized in Table 1.

**Table 1**
Physical and simulation parameters for balloon ascent modeling.

| Category | Parameter | Value | Unit |
|---|---|---|---|
| Balloon | Diameter $D$ | 5 | m |
| | Envelope mass $m_{\text{env}}$ | 5 | kg |
| | Payload mass $m_{\text{load}}$ | 5 | kg |
| Tether | Cross-section diameter $d$ | 0.006 | m |
| | Density $\rho_{\text{tet}}$ | 970 | kg/m$^3$ |
| | Segment length $K$ | 0.1 | m |
| | Elastic modulus $E$ | 95 | GPa |
| Wind | Reference wind speed $v_{\text{ref}}$ | 3 | m/s |
| | Reference height $H$ | 10 | m |
| | Ground altitude $h_{\text{ground}}$ | 0 | m |
| | Wind shear exponent $\alpha$ | 0.2 | – |
| Numerical Precision | Initial step | 1 | m |
| | Step factor | 0.01 | – |
| | Tolerance | 0.001 | m |

Given these physical parameters, the developed code is employed to simulate the ascent of the balloon by incrementally increasing its altitude $H$ from zero. At each step, the corresponding horizontal drift $X$ and tether length $L$ are computed. Since $H$, $X$, and $L$ are uniquely related through the quasi-static equilibrium of the system, any one of them can serve as the independent variable. To better reflect the practical process of balloon ascent–where the tether is gradually released–$L$ is chosen as the input parameter in the analysis, while the resulting balloon altitude $H$ and horizontal drift $X$ are recorded as outputs. Fig. 8(a) shows the variations of the horizontal drift $X$ and altitude $H$ of the balloon as functions of the released tether length $L$. It can be observed that the altitude increases rapidly at first and then approaches a plateau, whereas the horizontal drift increases slowly in the early stage and then grows more rapidly as the tether lengthens. Fig. 8(b) shows the tension force distribution along the tether during ascent. The blue and magenta solid curves represent the tension force profiles at released tether lengths of 1000 m and 1656.7 m, respectively. It is observed that the tension increases from the ground toward the top end attached to the balloon. As the tether is released, the maximum tension slightly decreases and eventually reaches a steady value. Fig. 8(c) illustrates the balloon's ascent path in black, while the colored curves indicate the tether profiles corresponding to released lengths of 1000 m and 1656.7 m, respectively. The color represents the tension stress distribution along the tether. The maximum tension stress reaches approximately 19.02 MPa, which is significantly lower than the failure strength of the UHMWPE tether material, i.e., 1.06 GPa. Finally, we would like to make two notes here. First, the numerical results obtained from the FEM approach are presented in Fig. 8(b) and (c) to verify the quasi-static equilibrium configuration of the tether. The close agreement between the FEM and analytical results confirms the validity and accuracy of the proposed force-based method. Second, the trends observed in ascent behavior and tension distribution are significantly influenced by key system parameters, including wind speed, balloon diameter, and tether length. The effects of these parameters will be analyzed in detail in the following sections.

## 5. Application

### 5.1. Parametric studies

With the method and simulation code described and validated above, the ascent of a given tethered balloon can be computed under user-specified wind conditions. The input parameters that govern the system's behavior include the balloon's geometric size (diameter), the total mass of the balloon and payload, and the tether's physical properties, such as density, cross-sectional diameter, and elastic modulus. Given these inputs, the code calculates the resulting balloon altitude and horizontal drift throughout the ascent. To further explore how these physical parameters influence the system's ascent behavior, we conduct a series of parametric studies in this section.

First, we investigate the ascent behavior of balloons with different sizes. Using a reference wind speed of 3 m/s, we vary the balloon diameter from 2.63 m to 10 m, while keeping all other parameters–such as the total mass of the balloon and the tether properties, as listed in Table 1–fixed. The results of this parametric study are shown in Fig. 9. The insets in Fig. 9 illustrate the variations of horizontal drift $X$ and altitude $H$ during ascent for balloon diameters of 5, 7, and 9 m. The figure reveals two key trends: (1) a balloon with a larger diameter can support a longer tether length, as expected, since a larger balloon generates greater net lift; and (2) for the same released tether length, a larger balloon reaches both a higher altitude and a greater horizontal drift. This behavior can be attributed to the fact that, as the balloon diameter increases, the drag force acting on it also increases. Thus, both net lift and aerodynamic drag emerge as dominant factors governing the ascent of the tethered balloon. Fig. 10 presents the variation of net lift and aerodynamic drag with respect to balloon diameter. As the diameter increases, both the net lift and drag increase; however, at higher altitudes, the net lift decreases more significantly than the drag. Consequently, while a larger balloon initially achieves greater altitude due to increased lift, the reduced lift at higher altitudes causes drag to play a more significant role–resulting in a larger horizontal drift.

Next, to further investigate the trade-off between net lift and aerodynamic drag on the balloon's altitude and horizontal drift, we analyze the effect of wind speed on the ascent behavior of the system while fixing the balloon diameter at 5 m. Fig. 11 shows the variation of net lift and drag forces for a 5-meter-diameter balloon under different reference wind speeds (1 m/s, 2 m/s, 3 m/s, 4 m/s, and 5 m/s). As the balloon ascends, the net lift gradually decreases due to the reduction in air density at higher altitudes; however, wind speed has no direct effect on the net lift. In contrast, the aerodynamic drag acting on the balloon increases significantly with higher wind speeds and continues to rise with altitude, driven by the increasing relative wind velocity. At lower wind speeds, net lift dominates, allowing the balloon to reach a higher altitude with relatively limited horizontal drift. Conversely, at higher wind speeds, drag becomes more significant, resulting in a greater horizontal displacement.

Fig. 12a-d show the ascent paths and intermediate tether shapes at different wind speeds ranging from 2 m/s to 4 m/s. The results are summarized in Fig. 13a. As wind speed increases, the tethered balloon reaches a lower altitude while exhibiting greater lateral drift. Fig. 13b presents the maximum tension and tension distribution along the tether for various wind speeds. As expected, the tension force increases progressively from the ground anchor to the balloon, since the uppermost point must support both the aerodynamic drag and the cumulative weight of the tether. Notably, the trend of maximum tension with respect to tether length varies with wind speed: at lower wind speeds, the maximum tension decreases as the released tether length increases, whereas at higher wind speeds, the maximum tension increases with tether length. This contrast reflects the competing effects of buoyancy, tether weight, and aerodynamic drag under different flow regimes.

### 5.2. Inverse design

Finally, inverse design is frequently used in practice to determine the appropriate configuration of a tethered balloon system in order to achieve a target drift and/or altitude. This can be accomplished by applying an optimization algorithm to a precomputed database generated using the simulation code. For example, Fig. 14a illustrates the resulting design parameters–balloon diameter and tether length–required to simultaneously achieve a specified drift and altitude. The method involves extracting the isolines corresponding to $X = 4000$ m and $H = 4000$ m from Fig. 9a and b, respectively, and identifying whether these two curves intersect. The intersection point represents the feasible design solution, yielding a balloon diameter of $D = 8.42$ m and a tether length of $L = 6029.4$ m, as shown in Fig. 14a. For the target values of $X = 2000$ m and $H = 1500$ m, no feasible design exists, as the corresponding isolines

do not intersect. In such cases, the nearest feasible design can be identified, as illustrated in Fig. 14b. This design suggests a balloon diameter of $D = 5.89$ m and a tether length of $L = 2674.3$ m, which results in a drift of $X = 1830.15$ m and an altitude of $H = 1677.04$ m. Fig. 14c showcases a specific case in which the tether length is fixed at $L = 267.0$ m and the target drift is $X = 150$ m. Under these conditions, the required balloon diameter is determined to be $D = 3.39$ m. Fig. 14d presents another case where the balloon has a fixed diameter of $D = 8$ m, and the objective is to achieve a target altitude of $H = 4000$ m. In this scenario, no exact solution exists. The nearest feasible solution corresponds to a tether length of $L = 5764.8$ m, which results in an actual altitude of $H = 3582.96$ m.

## 6. Conclusion

In this study, we developed a comprehensive simulation framework to model the ascent behavior of tethered balloons under various wind conditions. The method accounts for key physical parameters–including balloon geometry, payload mass, and tether properties–and accurately predicts the balloon's altitude, horizontal drift, tether shape and tether tension distribution throughout the ascent. To validate the computational accuracy of the results, a finite element model was also developed for simulating the behavior of a flexible, continuous tether. Through systematic parametric studies, we demonstrated how balloon size, tether length, and wind speed collectively influence ascent trajectories and tension profiles. Notably, we observed that larger balloons tend to reach higher altitudes and experience greater horizontal drift, while stronger wind leads to increased lateral drift and reduced altitude. The relative dominance of net lift and aerodynamic drag varies across different wind regimes, shaping the overall ascent behavior. Furthermore, we introduced an inverse design approach that enables the determination of balloon diameter and tether length required to achieve specified target altitudes and drifts. By leveraging a precomputed simulation database and isoline-matching techniques, we illustrated several representative design scenarios, including both exact solutions and nearest-feasible alternatives when exact targets could not be achieved.

The proposed methodology directly addresses gaps in the existing literature: it provides a computationally efficient means of predicting the ascent behavior of tethered balloons, validated against a continuous finite element model, offers an openly available MATLAB tool to support broader adoption, and extends current modeling capabilities with an inverse design strategy not previously available for tethered balloon systems. Together, these features establish the approach as a practical and flexible tool for both forward simulation and design applications, with particular impact on the rapid design and optimization of tethered balloon systems. At the same time, several limitations of the present work should be acknowledged. The model is developed specifically for spherical balloons and may not directly generalize to streamlined aerostats. The current approach assumes quasi-static ascent and simplified atmospheric conditions, excluding effects such as turbulence, humidity, and unsteady dynamics. Importantly, the validation performed here is numerical, and future work should incorporate experimental validation to assess real-world fidelity.

Future work may focus on incorporating unsteady wind fields, balloon deformation effects, and active control strategies to further enhance the model's fidelity and applicability. The proposed method is also readily extensible to simulate the ascent of tethered aerostats with arbitrary shapes, such as Helikites and airships, provided that the aerodynamic forces (e.g., lift and drag) are available through experimental measurements or computational fluid dynamics simulations. In such cases, the force balance must account for both translational and rotational equilibrium, and the placement of the tether attachment point(s), as well as the number of connecting tethers to the main line, becomes an important design consideration. Despite these complexities, the approach for calculating the tether shape and tension distribution remains consistent with the method presented in this work. Future extensions may also include the effects of cable vibrations, dynamic ascent in time-varying wind fields, and the stability of the aerostat under gust conditions. In a gusty environment, for example, a sudden increase in wind load on a portion of the tether would induce local deformation, which could then propagate along the tether. Under such dynamic conditions, it would be necessary to analyze wave propagation in the tether, as has been performed for space tether systems [44].

## CRediT authorship contribution statement

**Zhongwei Ni:** Writing – original draft, Methodology, Data curation; **Shiran Zhu:** Validation, Software, Data curation; **Shunan Dou:** Funding acquisition, Conceptualization; **Jiawei Song:** Funding acquisition, Conceptualization; **Ning An:** Writing – review & editing, Writing – original draft, Project administration, Formal analysis, Conceptualization.

## Data availability

I have shared the link to my data/code at the Data Availability via https://github.com/SCU-AN-Group/HATASIM.

## Declaration of competing interest

The authors declare that they have no known competing financial interests or personal relationships that could have appeared to influence the work reported in this paper.

## Acknowledgement

This research is supported by the National Natural Science Foundation of China (grant 12202295), the International (Regional) Cooperation and Exchange Projects of the National Natural Science Foundation of China (grant W2421002), and Sichuan Science and Technology Program (grant 2025ZNSFSC0845). Ning An, an Associate Professor at Sichuan University and currently a Guest Researcher at the University of Trento, gratefully acknowledges support from the China Scholarship Council (No. 202506240177).

## References

[1] G. Chen, Using a tethered balloon to monitor atmospheric water vapour dynamics over the Tibetan plateau, Nat. Rev. Earth Environ. 5 (2) (2024) 78–78.
[2] S.H. Alsamhi, F.A. Almalki, O. Ma, M.S. Ansari, M.C. Angelides, Performance optimization of tethered balloon technology for public safety and emergency communications, Telecommun. Syst. 75 (2) (2020) 235–244.
[3] S.A. Khaleefa, S.H. Alsamhi, N.S. Rajput, Tethered balloon technology for telecommunication, coverage and path loss, in: 2014 IEEE Students' Conference on Electrical, Electronics and Computer Science, IEEE, 2014, pp. 1–4.
[4] S.A. Alhusayni, S.K. Alsuwat, S.H. Altalhi, F.A. Almalki, H.S. Alzahrani, Experimental study of a tethered balloon using 5G antenna to enhance internet connectivity, in: Intelligent Computing: Proceedings of the 2021 Computing Conference, Volume 3, Springer, 2021, pp. 649–663.
[5] R.A. Borges, S. Battistini, C. Cappelletti, Yago, Altitude control of a remote-sensing balloon platform, Aerosp. Sci. Technol. 110 (2021) 106500.
[6] D. Zhang, H. Luo, Y. Cui, X. Zeng, S. Wang, Tandem, long-duration, ultra-high-altitude tethered balloon and its system characteristics, Adv. Space Res. 66 (10) (2020) 2446–2465.
[7] H. Zhang, R. Cai, Y. Yang, R. Zhao, Quasi-static numerical simulation of the dynamic launching process for high-altitude balloon, Aerosp. Sci. Technol. 117 (2021) 106830.
[8] S.H. Alsamhi, M.S. Ansari, O. Ma, F. Almalki, S.K. Gupta, Tethered balloon technology in design solutions for rescue and relief team emergency communication services, Disaster Med. Public Health Prep. 13 (2) (2019) 203–210.
[9] S.H. Alsamhi, M.S. Ansari, L. Zhao, S.N. Van, S.K. Gupta, A.A. Alammari, A.H. Saber, M.Y. Hebah, M.A.A. Alasali, H.M. Aljabali, et al., Tethered balloon technology for green communication in smart cities and healthy environment, in: 2019 First International Conference of Intelligent Computing and Engineering (ICOICE), IEEE, 2019, pp. 1–7.
[10] V. Gawande, P. Bilaye, A. Gawale, R. Pant, U. Desai, Design and fabrication of an aerostat for wireless communication in remote areas, in: 7th AIAA ATIO Conf, 2nd CEIAT Int'l Conf on Innov and Integr in Aero Sciences, 17th LTA Systems Tech Conf; Followed by 2nd TEOS Forum, 2007, p. 7832.
[11] K. Mahmood, N.A. Ismail, N.M. Suhadis, Tethered aerostat envelope design and applications: a review, in: AIP Conference Proceedings, 2226, AIP Publishing LLC, 2020, p. 050003.

[12] S.P. Jones, J.A. Krausman, Nonlinear dynamic simulation of a tethered aerostat, J. Aircr. 19 (8) (1982) 679–686.
[13] C. Williamson, R. Govardhan, Dynamics and forcing of a tethered sphere in a fluid flow, J. Fluids Struct. 11 (3) (1997) 293–305.
[14] R. Govardhan, C.H.K. Williamson, Vortex-induced motions of a tethered sphere, J. Wind Eng. Ind. Aerodyn. 69 (1997) 375–385.
[15] S. Zhu, R. Guo, X. Jin, X. Ma, J. Zhou, N. An, Form finding of cable-membrane structures with flexible frames: finite element implementation and application to surface accuracy analysis of umbrella-like rib-mesh reflectors, Adv. Eng. Softw. 198 (2024) 103789.
[16] G. Yang, D. Yang, Y. Zhang, J. Du, Form-finding design of cable-mesh reflector antennas with minimal length configuration, Aerosp. Sci. Technol. 63 (2017) 9–17.
[17] S. Badesha, J. Bunn, Dynamic simulation of high altitude tethered balloon system subject to thunderstorm windfield, in: AIAA Atmospheric Flight Mechanics Conference and Exhibit, 2002, p. 4614.
[18] P. Coulombe-Pontbriand, M. Nahon, Experimental testing and modeling of a tethered spherical aerostat in an outdoor environment, J. Wind Eng. Ind. Aerodyn. 97 (5–6) (2009) 208–218.
[19] G.S. Aglietti, Dynamic response of a high-altitude tethered balloon system, J. Aircr. 46 (6) (2009) 2032–2040.
[20] S. Redi, G.S. Aglietti, A.R. Tatnall, T. Markvart, Dynamic response to turbulence of tethered lighter-than-air platforms, J. Aircr. 48 (2) (2011) 540–552.
[21] N.N. Smirnov, Y.A. Demyanov, A.V. Zvyaguin, A.A. Malashin, A.A. Luzhin, Dynamical simulation of tether in orbit deployment, Acta Astronaut. 67 (3–4) (2010) 324–332.
[22] A.A. Malashin, N.N. Smirnov, O.Y. Bryukvina, P.A. Dyakov, Dynamic control of the space tethered system, J. Sound Vib. 389 (2017) 41–51.
[23] P.A. Diakov, A.A. Malashin, N.N. Smirnov, Problem of load transportation along a space tethered system, Acta Astronaut. 150 (2018) 44–48.
[24] P.A. Diakov, A.A. Malashin, N.N. Smirnov, Dynamic processes in the tether of a space tethered system, Acta Astronaut. 163 (2019) 100–106.
[25] P.A. Diakov, A.A. Malashin, N.N. Smirnov, Estimation of parameters of the space tethered system for stable load transportation along the tether, Acta Astronaut. 181 (2021) 602–605.
[26] S.P. Jones, L.D. Schroeder, Nonlinear dynamic simulation of a tethered aerostat: a fidelity study, J. Aircr. 38 (1) (2001) 64–68.
[27] A. Howard, Experimental characterization and simulation of a tethered aerostat with controllable tail fins (2008). https://escholarship.mcgill.ca/concern/theses/cj82kb07h.
[28] C. Lambert, M. Nahon, D. Chalmers, Study of a multitethered aerostat system: experimental observations and model validation, J. Aircr. 43 (4) (2006) 1182–1189.
[29] R. Farley, Balloonascent: 3-D simulation tool for the ascent and float of high-altitude balloons, in: AIAA 5th ATIO and 16th Lighter-Than-Air Sys Tech. and Balloon Systems Conferences, 2005, p. 7412.
[30] K. Mahmood, N.A. Ismail, Application of multibody simulation tool for dynamical analysis of tethered aerostat, J. King Saud Univer. Eng. Sci. 34 (3) (2022) 209–216.
[31] F. Deschesnes, M. Nahon, Design improvements for a multi-tethered aerostat system, in: AIAA Atmospheric Flight Mechanics Conference and Exhibit, 2005, p. 6126.
[32] A. Sasidharan, R.K. Velamati, A. Mohammad, S. Benaissa, Mathematical modelling of a single tethered aerostat using longitudinal stability derivatives, Sci. Rep. 14 (1) (2024) 3697.
[33] B. Hembree, N. Slegers, Tethered aerostat modeling using an efficient recursive rigid-body dynamics approach, J. Aircr. 48 (2) (2011) 623–632.
[34] W. Kang, I. Lee, Analysis of tethered aerostat response under atmospheric turbulence considering nonlinear cable dynamics, J. Aircr. 46 (1) (2009) 343–348.
[35] M. Cavcar, The international standard atmosphere (ISA), Anadolu Univer. Turk. 30 (9) (2000) 1–6.
[36] F.M. White, J. Majdalani, Viscous Fluid Flow, 3, McGraw-Hill New York, 2006.
[37] P. Coulombe-Pontbriand, M. Nahon, Experimental characterization and simulation of a tethered spherical helium balloon in an outdoor environment, in: AIAA 5th ATIO and16th Lighter-Than-Air Sys Tech. and Balloon Systems Conferences, 2005, p. 7390.
[38] B.R. Munson, T.H. Okiishi, W.W. Huebsch, A.P. Rothmayer, Fundamentals of Fluid Mechanics, Wiley, 2013. https://books.google.co.jp/books?id=R17cthBdckYC.
[39] Z.-G. Feng, E.E. Michaelides, Drag coefficients of viscous spheres at intermediate and high Reynolds numbers, J. Fluids Eng. 123 (4) (2001) 841–849.
[40] H. Yang, M. Fan, A. Liu, L. Dong, General formulas for drag coefficient and settling velocity of sphere based on theoretical law, Int. J. Mining Sci. Technol. 25 (2) (2015) 219–223.
[41] H. Schlichting, K. Gersten, Boundary-Layer Theory, springer, 2016.
[42] J. Happel, H. Brenner, Low Reynolds Number Hydrodynamics: with Special Applications to Particulate Media, 1, Springer Science & Business Media, 2012.
[43] A.H. Pevrot, A.M. Goulois, Analysis of cable structures, Comput. Struct. 10 (5) (1979) 805–813.
[44] P. Diakov, A.A. Malashin, N.N. Smirnov, S.A. Tarasov, Peculiarities of wave dynamics in the tether of a space tethered system, Acta Astronaut. 194 (2022) 425–433.